Biomaterials 35 (2014) 344–355

Contents lists available at ScienceDirect

Biomaterials

journal homepage: www.elsevier.com/locate/biomaterials

# Self-assembled magnetic fluorescent polymeric micelles for magnetic resonance and optical imaging

Kai Yan [a,1], Huan Li [b,1], Penghui Li [c], Haie Zhu [a], Jie Shen [d], Changfeng Yi [a,d], Shuilin Wu [a,c], Kelvin W.K. Yeung [d], Zushun Xu [a,c,***], Haibo Xu [b,**], Paul K. Chu [c,*]

[a] Ministry of Education Key Laboratory for The Green Preparation and Application of Functional Materials, Hubei University, Wuhan, Hubei 430062, China
[b] Department of Radiology at Union Hospital, Tongji Medical College of Huazhong University of Science and Technology, Wuhan, Hubei 430030, China
[c] Department of Physics and Materials Science, City University of Hong Kong, Tat Chee Avenue, Kowloon, Hong Kong, China
[d] Department of Orthopaedics and Traumatology, The University of Hong Kong, Pokfulam Road, Hong Kong, China

ARTICLE INFO

*Article history:*
Received 18 August 2013
Accepted 10 September 2013
Available online 5 October 2013

*Keywords:*
Self-assembly
Amphiphilic copolymer
Magnetic nanoparticles
Magnetic resonance imaging
Optical imaging

ABSTRACT

Stable and cytocompatible hybrid PEGylated micelles with multimodal imaging capabilities are described. The $F_3O_4$-encapsulated polymeric micelles composed of cores containing magnetic nanoparticles and polyethylene glycol (PEG) shells are synthesized by self-assembly of amphiphilic poly(-HFMA-co-VBK)-g-PEG copolymers and oleic acid stabilized $Fe_3O_4$ nanoparticles. The $Fe_3O_4$ magnetic nanoparticles in the core produce $T_2$-weighted MR imaging functionalities, whereas the small fluorescent monomer carbazole in the polymer shell introduces good fluorescent properties. The multifunctional micelles exhibit excellent paramagnetic properties with the maximum saturation magnetization of 9.61 emu/g and transverse relaxivity rate of 157.44 $m_M^{-1}$ $S^{-1}$. *In vivo* magnetic resonance imaging (MRI) studies reveal enhanced contrast between the liver and spleen. Fluorescence spectra show characteristic emission peaks from carbazole at 350 nm and 365 nm and vivid blue fluorescence can be observed by 2-photon confocal scanning laser microscopy (CLSM). *In vivo* optical imaging demonstrates the unique fluorescent characteristics of the $Fe_3O_4$-encapsulated polymeric micelles in the liver and spleen and the excellent multifunctional properties suggest potential clinical use as nanocarriers in magnetic resonance imaging and optical imaging.



## 1. Introduction

The emergence of nanotechnology and biotechnology has created an exciting and interdisciplinary area of nanobiotechnology [1–3]. Multifunctional nanocarriers possess favorable properties integrated into a single nanosystem spurring new applications such as multimodal imaging and simultaneous diagnosis and therapy [4–6]. As diagnostic techniques, they have been explored in magnetic resonance imaging (MRI), computed tomography (CT), positron emission tomography (PET), optical imaging, and so on [7,8]. However, most of them have drawbacks such as low sensitivity, weak penetrability, and insufficient spatial or temporal resolution [9–11] and there have been attempts to combine two or more imaging modalities to improve the performance [12,13], for instance, PET/CT [14], MRI/CT [15], MRI/PET [16], and MRI/optical imaging [17–21]. One of the popular approaches is to combine the MRI and optical imaging modalities [22]. MR imaging offers high spatial resolution and the capacity to simultaneously obtain physiological and anatomical information in living organisms based on the interactions between protons and molecules in the surrounding tissues, whereas optical imaging allows rapid screening [23,24].

Magnetic resonance imaging (MRI) is one of the most useful diagnostic techniques providing noninvasive and real-time detection of diseases and super-paramagnetic nanoparticles are excellent contrast agents capable of noninvasive monitoring of pathological changes on both the molecular and cellular levels *in vivo* [25,26]. However, magnetic nanoparticles are commonly stabilized with oleic acid and their biological applications are hampered because of the poor dispersion properties in blood [27,28]. Several strategies such as ligand exchange [29] and self-assembly [30,31] have been proposed to enhance their water

* Corresponding author. Tel.: +852 34427724; fax: +852 34420542.
** Corresponding author. Tel.: +86 2785726410; fax: +86 2785726919.
*** Corresponding author. Ministry of Education Key Laboratory for The Green Preparation and Application of Functional Materials, Hubei University, Wuhan, Hubei 430062, China. Tel.: +86 2788661897; fax: +86 2788665610.
*E-mail addresses:* zushunxu@hubu.edu.cn (Z. Xu), xuhaibo1120@hotmail.com (H. Xu), paul.chu@cityu.edu.hk (P.K. Chu).
[1] These two authors contributed equally to this project.

0142-9612/$ – see front matter © 2013 Elsevier Ltd. All rights reserved.
http://dx.doi.org/10.1016/j.biomaterials.2013.09.035

solubility. In particular, amphiphilic polymers produced by controlled radical polymerization for magnetic nanoparticle encapsulation exhibit good colloidal stability compared to small molecule surfactants [32,33]. Kim et al. reported amphiphilic poly(styrene$_{250}$-block-acrylic acid$_{13}$) ($PS_{250}$-b-$PAA_{13}$) copolyolefin with magnetic nanoparticles to enclose the particles in the copolymer micelles. They demonstrated that the surrounding polymer could be cross-linked to fix the nanostructures topologically and these structures were stable to subsequent synthetic transformation of surface functional groups [34]. Ai et al. showed that oleic acid and oleylamine modified magnetic particles could be encapsulated inside the hydrophobic core of poly(-caprolactone)-b-poly(ethylene glycol)(PCL-b-PEG) micelles by ring-opening polymerization [35].

Fluorescent nanomaterials comprising π-conjugated polymers have attracted much interest lately due to their small size as well as high fluorescence and photochemical stability which render them appealing as bioprobes in labeling and imaging [36]. For example, carbazole and their derivatives have a large conjugated system, photoconductive feature, and strong intramolecular electron transfer and are excellent optical materials [37]. Li prepared water-soluble trifunctional nanoparticles with thermoresponsive, magnetic, and fluorescent hybrid *via* surface-initiated reversible addition–fragmentation chain transfer (RAFT) polymerization. They used the fluorescent RAFT agent with carbazole as the chain transfer agent, which could enhance the negative contrast in MRI [38].

In our previous work, we demonstrated the preparation of magnetite ($Fe_3O_4$)-loaded polymer micelles by self-assembly of fluorine-containing amphiphilic poly(HFMA-g-PEGMA) copolymers with oleic acid modified $Fe_3O_4$ nanoparticles in an aqueous medium [39]. However, the single imaging modality could not convey all the necessary information about the biological structure and functions of an organ. Herein, a dual-modality imaging probe is designed and fabricated and *in vivo* optical imaging and MRI experiments demonstrate their suitability as $T_2$-weighted negative MRI contrast agents and fluorescent probes in liver and spleen imaging.

## 2. Materials and methods

### 2.1. Materials

2,2,3,4,4,4-Hexafluorobutyl methacrylate (HFMA) purchased from Xeogia Fluorine–Silicon Chemical Company (Harbin, China, Chemical Purity) was distilled at reduced pressure before use. Methoxy poly(ethylene glycol) monomethacrylate (PEGMA) (average $M_n$ 950 g/mol) was obtained from Aldrich and used without further purification and 2,2′-azobisisobutyronitrile (AIBN, analytical grade) was purified by recrystallization in ethanol. 4-Vinylbenzyl chloride (90%) and carbazole (≥95%) were supplied by Aldrich Chemical Company. Potassium iodide (KI), oleic acid (OA, analytical reagent), sodium hydroxide (NaOH), iron (III) chloride hexahydrate ($FeCl_3 \cdot 6H_2O$), iron (II) chloride tetrahydrate ($FeCl_2 \cdot 4H_2O$), ammonium hydroxide ($NH_3 \cdot H_2O$, 25–28%), ethanol, hexane, N,N-dimethylformamide (DMF, analytical reagent), and tetrahydrofuran (THF, analytical reagent) were purchased from Sinopharm Chemical Reagent Co., Ltd., China and 3-(4,5-dimethyl thiazol-2-yl)-2,5-diphenyl tetrazolium bromide (MTT) were bought from Sigma–Aldrich.

### 2.2. Synthesis of 9-(4-vinylbenzyl)-9H-carbazole (VBK)

The fluorescent monomer VBK was synthesized according to that described in the literature with some modifications [40] as shown in Scheme 1. Succinctly speaking, 2.11 g of carbazole and 0.63 g of NaOH were dissolved in 30 mL of DMF together with 0.05 g of KI as the catalyst under vigorous magnetic stirring for 3 h. 2.34 g of 4-vinylbenzyl chloride was dripped slowly into the mixture at room temperature (RT) and after stirring for 20 h at room temperature, the mixture was poured into a large amount of deionized water. The crude product was precipitated and collected by filtration and while crystals were produced by recrystallization in acetone.

### 2.3. Preparation of iron oxide nanoparticles

Mono-dispersed super-paramagnetic iron oxide nanoparticles were prepared by chemical co-precipitation, followed by modification with oleic acid [41]. 26.115 g of $FeCl_3 \cdot 6H_2O$ and 13.31 g of $FeCl_2 \cdot 4H_2O$ were mixed in 160 mL of deoxygenated water in a 500 mL three-necked flask. The solution was stirred under nitrogen for 0.5 h and 90 mL of $NH_3 \cdot H_2O$ was added drop-wise to obtain a pH value of 10–11 in order to produce black precipitates and allow the growth of iron oxide nanoparticles. The solution was heated to 75 °C for 1 h and 9 g of oleic acid were added drop by drop at a constant rate and the reaction proceeded for another hour. Afterwards, the black mixture was cooled and washed by repeated dispersion and precipitation with hexane and ethanol, respectively. The final product was dispersed in hexane and the resulting ferrofluid was sealed in a glass vial for storage.

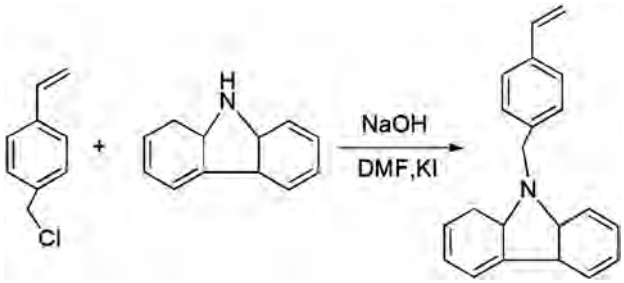


**Scheme 1.** Schematic illustration of the preparation fluorescent monomer VBK.

### 2.4. Synthesis of amphiphilic poly(HFMA-co-VBK)-g-PEG copolymers

The amphiphilic poly(HFMA-co-VBK)-g-PEG copolymers were synthesized by free radical polymerization as described in our previous paper [42]. Briefly, 1.005 g of PEGMA, 0.815 g of HFMA, and 0.102 g of VBK were dissolved in 12 mL of THF. After adding 0.068 g of AIBN as the radical initiator, the mixture was transferred to a 50 mL round-bottom flask with a magnetic stirrer and degassed by bubbling with $N_2$ several times in an ice bath. Polymerization proceeded at 75 °C for 24 h and the amphiphilic poly(HFMA-co-VBK)-g-PEG copolymers were collected by precipitation in hexane thrice. The purified products were dried under vacuum at 35 °C for later use.

### 2.5. Preparation of $Fe_3O_4$-encapsulated polymeric micelles

The amphiphilic poly(HFMA-co-VBK)-g-PEG copolymers were dissolved in 25 mL of distilled water and mixed with the oleic acid stabilized $Fe_3O_4$ nanoparticles (0.210 g) in hexane. The two-phase suspension was vigorously sonicated at 70 °C for 20 min under nitrogen bubbling to evaporate the hexane and produce the self-assembled micelles. The colloids underwent centrifugation and the collected $Fe_3O_4$-encapsulated polymeric micelles were washed three times with distilled water to remove the unbound polymer.

### 2.6. Effects of HFMA/(PEGMA + VBK) ratio on $Fe_3O_4$ loading efficiency

To optimize the $Fe_3O_4$ loading efficiency, a series of poly(HFMA-co-VBK)-g-PEG samples with variable HFMA/(PEGMA + VBK) mass ratios from 0.258/(1.004 + 0.101) to 1.516/(1.004 + 0.101) were synthesized. The oleic acid stabilized $Fe_3O_4$ nanoparticles were added to the amphiphilic copolymers at the same ratio described in Section 2.5. Here, the abbreviation scheme PEG–VBK–$F_x$ is used, where *X* represents the HFMA wt% in the amphiphilic copolymer. For example, PEG–VBK–$F_{42.4}$ is the amphiphilic copolymer with 42.4 wt% of HFMA in the backbones. The samples were lyophilized and the $Fe_3O_4$ loading efficiency was evaluated by atomic absorption spectrophotometry (AA-680).

### 2.7. In vitro cytotoxicity

The cytotoxicity of the $Fe_3O_4$-encapsulated polymeric micelles was assessed by the MTT assay. HeLa cells were placed on the wells ($10^4$ cells per well) of 96-well plates, grown for 24 h, washed with PBS (pH = 7.4), and incubated with different concentrations of $Fe_3O_4$-encapsulated polymeric micelles (dose diluted by complete medium, 0–1000 μg/mL) for another 24 h. Afterwards, the supernatants were removed and cells were washed with PBS (pH = 7.4) three times. 40 μL of the MTT solution (2.5 mg $mL^{-1}$) were added to each well and after incubation for 4 h, the culture medium was discarded. Each well received 100 μL of DMSO and vigorous pipetting for 3–5 min to dissolve the precipitates. The absorption peak at 570 nm was measured on a microplate reader and data from six parallel wells were averaged to obtain the result for each sample. The relative cell viability was calculated by the following equation: Relative cell viability (%) = ($OD_{treated}/OD_{control}$) × 100%, where $OD_{treated}$ was obtained in the presence of the $Fe_3O_4$-encapsulated polymeric micelles and $OD_{control}$ was obtained without the $Fe_3O_4$-encapsulated polymeric micelles and defined as 100% viability.

### 2.8. In vitro MRI characterization and in vivo MRI

To determine the relaxivity, the $Fe_3O_4$-encapsulated polymeric micelles were diluted with distilled water containing iron concentrations in the range of 0.015–0.16 mmol/L. The samples were transferred to a series of 600-μL sample tube, placed in an MR scanner, and tested based on a number of MR sequences. The $T_2$ relaxation time of the suspension was computed using the in-house software (MATLAB V7.1) and the relaxivity values of $r_2$ were calculated by fitting the $1/T_2$ relaxation time versus Fe concentration (mM) curve.

The *in vivo* MRI studies were performed on SD mice (weight of approximately 240 g). All the animals were managed and treated according to the rules and regulations of the Institutional Animal Care and Use Committee at Hubei University, and the animal protocols were also approved by the Institutional Animal Care. The mice were anaesthetized by trichloroacetaldehyde hydrate (10%) with a dose of 45 mg/kg at normal body temperature. The mice were scanned before and after administration of 1.5 mL of the $Fe_3O_4$-encapsulated polymeric micelles with a dose of 6 mg (Fe)/kg through the tail vein for 4 h. The $T_2$-weighted coronal MR images were acquired from the MR scanner. The signal intensity (SI) was measured at each time point and the relative SI changes were plotted versus time. The relative signal enhancement values (RSEs) were calculated using SI measurements before ($SI_{pre}$) and after ($SI_{post}$) injection of the contrast agents based on the following formula: $[(SI_{post} - SI_{pre})/SI_{pre}] \times 100\%$. The $SI_{post}$ values were determined at time points of 30 min, 60 min, 120 min, 180 min, and 240 min.

### 2.9. Histological analysis

The mice were sacrificed 10 h after injection with the $Fe_3O_4$-encapsulated polymeric micelles. The liver, spleen, kidney, and muscle were fixed in 4% paraformaldehyde for 24 h and transferred to 30% sucrose in the PBS buffer. The tissues were prepared for histological analysis by Prussian blue staining (iron staining). In the pathological analysis, the slides of liver and spleen were prepared for confocal laser scanning microscopy (CLSM).

### 2.10. Characterization

$^1$H NMR was used to determine the chemical structure of VBK and amphiphilic poly(HFMA-co-VBK)-g-PEG copolymers. It was conducted on the UNITY INVOA 600 MHz spectrometer (Varian, USA) with DMSO-d6 and $CDCl_3$ as the solvent. Fourier transform infrared spectroscopy (FTIR) was carried out on the Perkin Elmer Spectrum one Transform Infrared spectrometer (USA). The dried samples (oleic acid stabilized $Fe_3O_4$ nanoparticles, amphiphilic poly(HFMA-co-VBK)-g-PEG copolymers, and $Fe_3O_4$-encapsulated polymeric micelles) were pressed with KBr into compact pellets. The number-average molecular weight ($M_n$), weight-average molecular weight ($M_w$) and polydispersity index (PDI) were measured by gel permeation chromatography (GPC) utilizing the 1515 pump. The morphology of the nanoparticles (oleic acid stabilized $Fe_3O_4$ nanoparticles, amphiphilic poly(HFMA-co-VBK)-g-PEG copolymer micelles, and $Fe_3O_4$-encapsulated polymeric micelles) was examined by transmission electron microscopy (TEM, Tecnai G20, FEI Corp., USA) at an accelerating voltage of 200 kV. The hydrodynamic size and size distribution of the samples were characterized by dynamic light scattering (DLS, Autosize Loc-Fc-963, Malvern Instrument). The excitation and emission spectra of the amphiphilic poly(HFMA-co-VBK)-g-PEG copolymer micelles and $Fe_3O_4$-encapsulated polymeric micelles were measured on an F-2500 spectrometer (Hitachi High Technologies Corporation, Japan). The CLSM images of the amphiphilic poly(HFMA-co-VBK)-g-PEG copolymer micelles, liver, and spleen were obtained on the Spectra Physics MaiTai HP tunable 2-photon (690–1040 nm) laser confocal microscopy (Carl Zeiss LSM710) using 2-photon laser excitation at 690 nm. The XRD (X-ray diffraction) spectra of the oleic acid stabilized $Fe_3O_4$ nanoparticles and $Fe_3O_4$-encapsulated polymeric micelles were acquired on the X'PertPro (Philips Corp., Nederland) using Cu Kα radiation at a scanning rate of 10°/min from 20° to 80°. The magnetic properties were studied using a vibrating sample magnetometer (VSM, HH-15, China) at 298 K under an applied magnetic field. The thermogravimetric analysis was performed on the Perkin Elmer TGA-7 and the dried powder samples were heated at the rate 10 °C/min from 50 °C to 600 °C in a nitrogen atmosphere.

Both the *in vitro* and *in vivo* MRI experiments were performed at 25 °C using a 3.0 T whole-body MR scanner (MAGNETOM Trio, A Tim System 3T, Siemens, Munich, Germany) in combination with an 8-channel wrist joint coil. In the *in vitro* MRI experiment, the following parameters were adopted: field of view (FOV) = 120 mm, base resolution = 384 × 384, slice thickness = 1.5 mm, multiple echo times (TE) = 20, 40, 60, 80, 100, 120, and 140 ms, repetition time (TR) = 2000 ms, and scanned time = 13–14 min. The Fe concentration of the micelles in water was determined by atomic absorption spectrophotometry (AA-680) after dissolving the micelles in a solution of $HNO_3/HClO_4$ at 150 °C. In the *in vivo* MRI experiments, the field of view (FOV) was 100 nm, base resolution was 192 × 192, slice thickness was 3.0 mm, multiple echo time (TE) was 62 ms, repetition time (TR) was 3000 ms, and flip angle was 120°.

## 3. Results and discussion

The process to synthesize the $Fe_3O_4$-encapsulated polymeric micelles is illustrated in Scheme 2. The super-paramagnetic iron oxide nanoparticles, which are frequently used as contrast agents in MRI, are produced by chemical co-precipitation and then modified

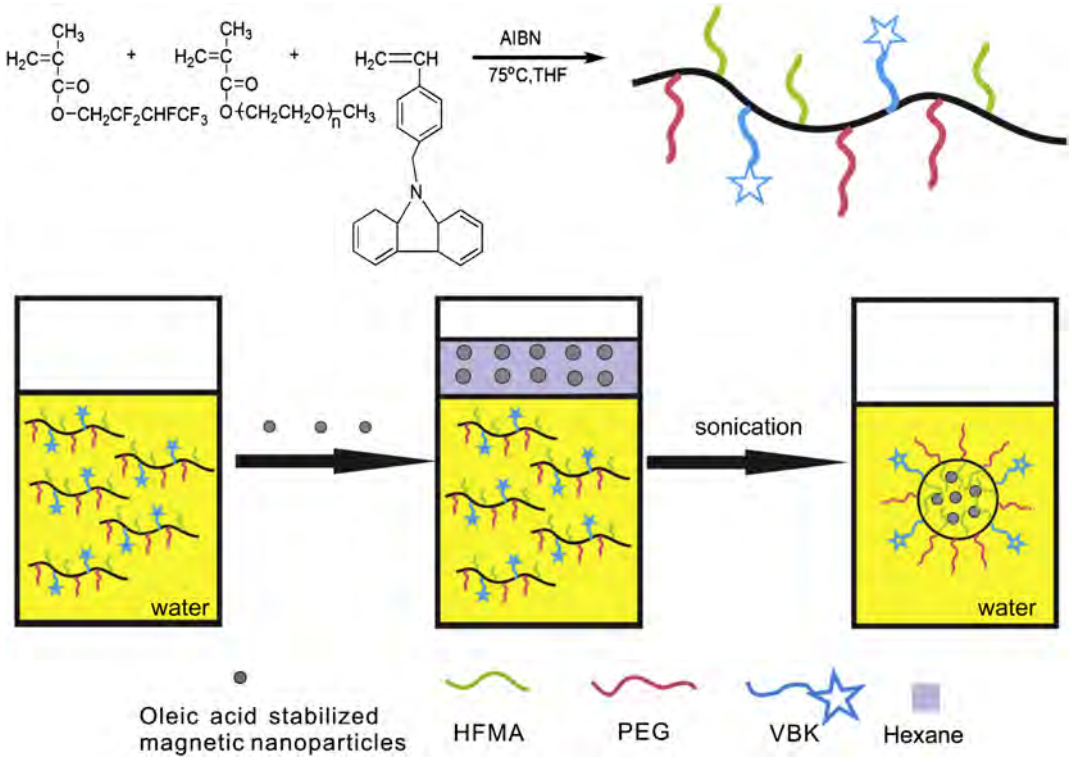


**Scheme 2.** Schematic illustration of the preparation of the magnetic fluorescent polymeric micelles encapsulated with magnetic nanoparticles by self-assembly.

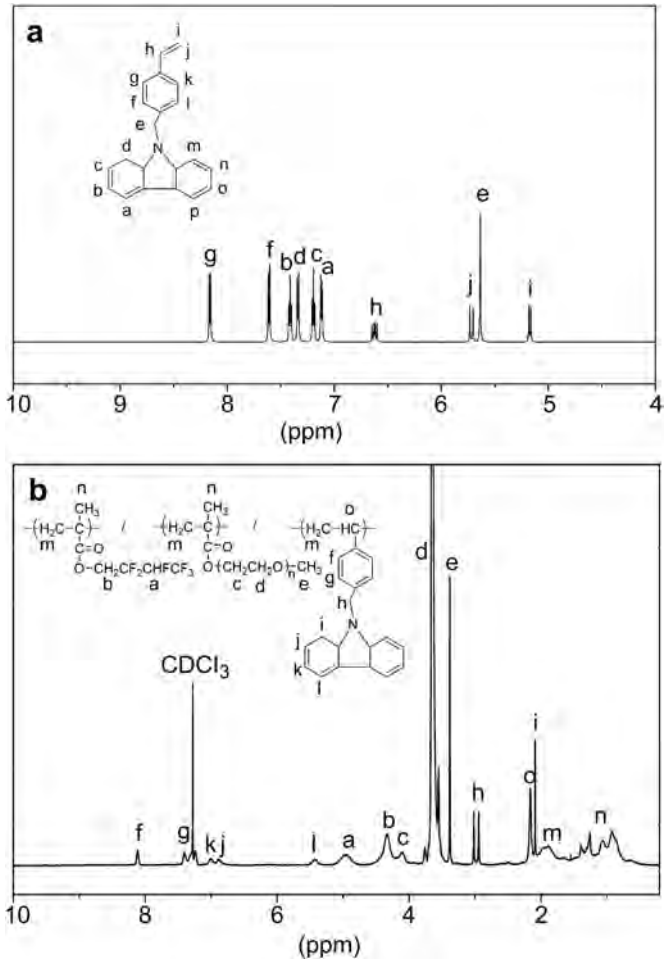


**Fig. 1.** $^1$H NMR spectra: (a) Fluorescent monomer VBK and (b) Amphiphilic poly(-HFMA-co-VBK)-g-PEG copolymers.

with oleic acid to enhance dispersion in hexane. The amphiphilic fluorescent poly(HFMA-co-VBK)-g-PEG copolymers are prepared by polymerization of the hydrophobic HFMA monomers, hydrophilic PEGMA macromonomers, and fluorescent monomers VBK in THF at 75 °C. Generally, amphiphilic polymers which form micelles

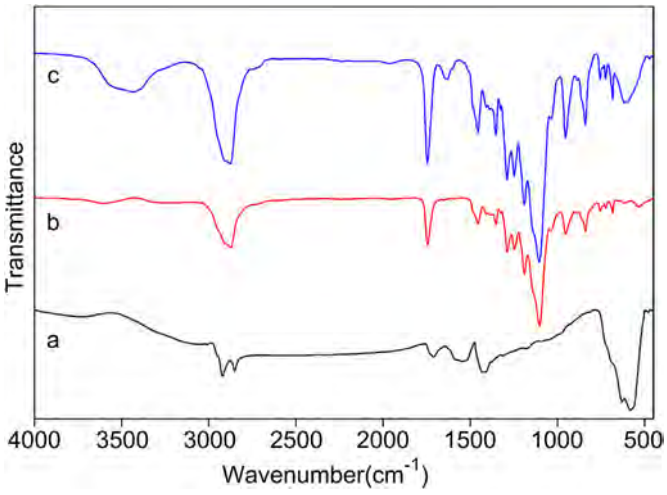


**Fig. 2.** FTIR spectra: (a) Oleic acid stabilized $Fe_3O_4$ nanoparticle, (b) Amphiphilic poly(HFMA-co-VBK)-g-PEG copolymers, and (c) $Fe_3O_4$-encapsulated polymeric micelles.

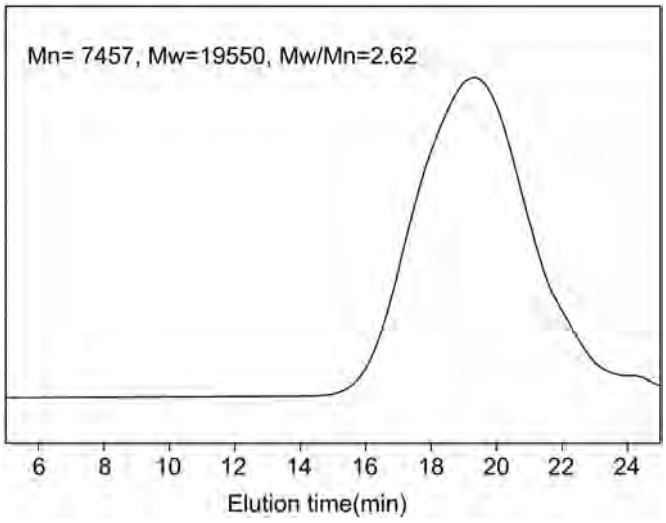


**Fig. 3.** Typical GPC curve of the amphiphilic poly(HFMA-co-VBK)-g-PEG copolymers (HFMA/(PEGMA + VBK) = 0.815/(1.005 + 0.102)).

in water *via* self-assembly can encapsulate the hydrophobic gust molecules [43]. In this approach, the hydrophobic fluorocarbon segments are inserted into the oleic acid shell of the magnetic nanoparticles with the hydrophilic parts on the surface forming the water-soluble nanocomposites after evaporation of hexane. The water-soluble nanocomposites are stable in neutral aqueous solutions and suitable for biomedical applications.

### 3.1. Synthesis and characterization of fluorescent monomer VBK and amphiphilic poly(HFMA-co-VBK)-g-PEG copolymers

Scheme 1 shows the fluorescent monomer VBK synthesis pathway. A new type of fluorescent monomer VBK is synthesized by Michael-type reaction and the amphiphilic fluorescent poly(-HFMA-co-VBK)-g-PEG copolymers are prepared by radical polymerization in THF using AIBN as the initiator. The chemical structures are determined by $^1$H NMR and Fig. 1a shows the spectrum of the fluorescent monomer VBK. The characteristic signals of VBK are: (a & p, $\delta$ = 7.12 ppm), (b & o, $\delta$ = 7.42 ppm), (c & n, $\delta$ = 7.21 ppm), (d & m, $\delta$ = 7.34 ppm), (e, $\delta$ = 5.63 ppm), (f & l, $\delta$ = 7.61 ppm), (g & k, $\delta$ = 8.15 ppm), (h, $\delta$ = 6.62 ppm), (I,

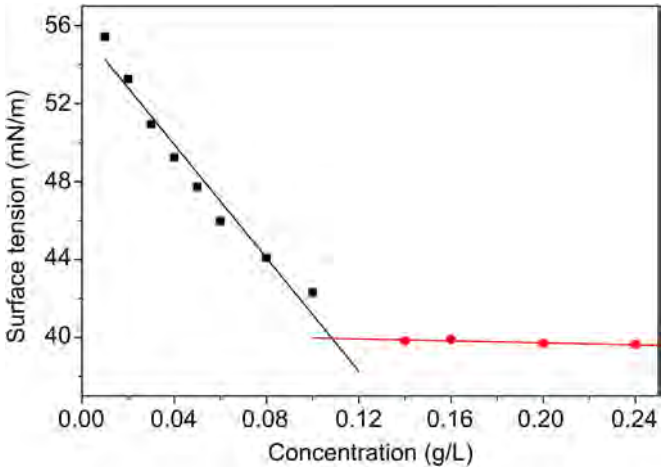


**Fig. 4.** Critical micelle concentrations of the amphiphilic poly(HFMA-co-VBK)-g-PEG copolymers.

$\delta$ = 5.17 ppm), (j, $\delta$ = 5.72 ppm). In comparison with the $^1$H NMR spectrum of the VBK shown in Fig. 1a, several new peaks can be observed from the amphiphilic copolymer and they can be ascribed to the protons of the HFMA and PEGMA segments. The characteristic signals of the PEG graft chains consist of the broad peak at $\delta$ = 3.63 ppm (d) assigned to $-CH_2CH_2O-$, the peak at $\delta$ = 4.09 ppm (c) belonging to the repeating units of the PEG segment, and the singlet at $\delta$ = 3.38 ppm (a) assigned to $-OCH_3$. The characteristic signals of the fluorinated HFMA segments include the peaks at $\delta$ = 4.33 ppm (b) assigned to $-CH_2CF_2-$ and $\delta$ = 4.95 ppm (a) corresponding to $-CHFCF_3$ of the HFMA segment. In addition, the signal at 1.92 ppm (m) is associated with $-CH_2-$ of the copolymer backbone and that at 0.82–1.32 ppm (n) is attributed to $-CH_3$ linked to the backbone.

Fig. 2b shows the FTIR spectrum of the amphiphilic poly(HFMA-co-VBK)-g-PEG copolymers. The characteristic strong absorption of ester carbonyl (C=O) bands in HFMA and PEG appears at 1745 cm$^{-1}$ and the peak at 1189 cm$^{-1}$ is assigned to absorption by the C–F groups. The strong peak at 1102 cm$^{-1}$ is attributed to absorption by the ether bands (C–O) in PEG, the broad peak at 2889 cm$^{-1}$ arises from to $-CH_3$ and $-CH_2-$groups and that at 1455 cm$^{-1}$ stems from aromatic groups in the chain of VBK.

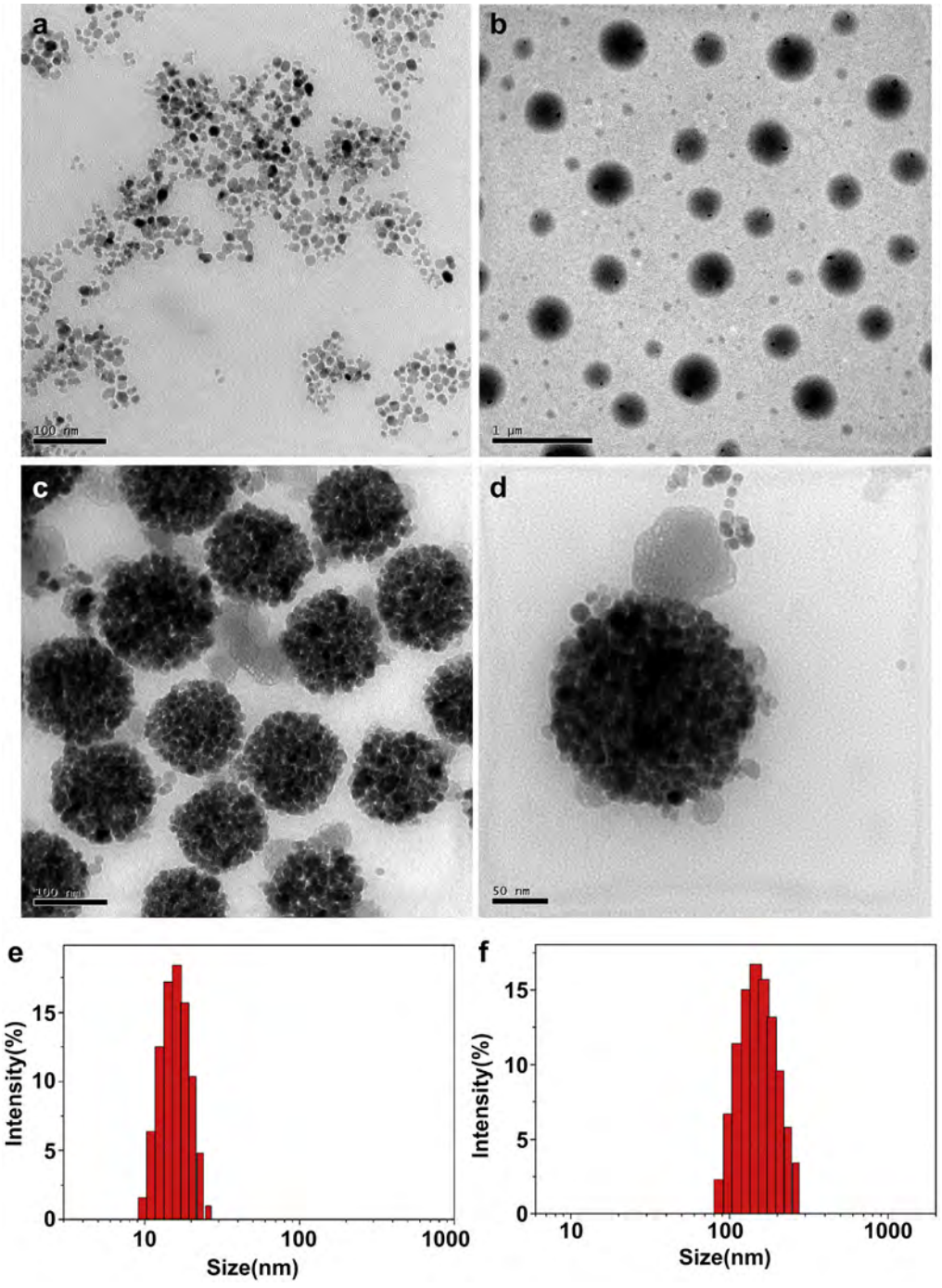


**Fig. 5.** TEM images: (a) Oleic acid stabilized $Fe_3O_4$ nanoparticles in hexane, (b) Amphiphilic poly(HFMA-co-VBK)-g-PEG copolymers in water, (c) and (d) $Fe_3O_4$-encapsulated polymeric micelles in water with different rear views, Size distribution of (e) oleic acid stabilized $Fe_3O_4$ nanoparticles in hexane and (f) hybrid micelles in water.

The molecular weight and molecular weight distribution of the amphiphilic poly(HFMA-co-VBK)-g-PEG copolymers are determined by GPC. The chromatograms are shown in Fig. 3. The elution peaks of typical amphiphilic poly(HFMA-co-VBK)-g-PEG copolymers are relatively mono-modal and symmetric showing no evident shoulders or tails on both the lower and higher molecular weight sides.

For amphiphilic surfactants in an aqueous solution, the hydrophilic portions often submerge in water while the hydrophobic portions extend into air to reduce the surface tension. When the concentration increases to a certain point, the surface tension of the solution no longer decreases, and many micelles form. The concentration at which the surfactant forms micelles is called the critical micelle concentration (CMC) [44]. In order to determine the critical micelle concentration of amphiphilic poly(HFMA-co-VBK)-g-PEG copolymers, the surface tension of the solutions with different concentrations is measured. Fig. 4 shows a linear decrease in the surface tension with increasing concentration but it is flat at high concentrations. The critical micelle concentration determined from the intersection of the two lines is 0.108 g/L.

### 3.2. Synthesis and characterization of iron oxide nanoparticles and $Fe_3O_4$-encapsulated polymeric micelles

The iron oxide nanoparticles are produced by co-precipitation of $Fe^{2+}$ and $Fe^{3+}$ in an aqueous solution to which ammonium hydroxide is added. Oleic acid produces high affinity to iron oxide through the chemical interaction between the −COO group and Fe atoms. As a result, the hydrophobic tail of the oleic molecule points outward to generate a nonpolar shell and the oleic acid stabilized magnetic nanoparticles can dissolve in hexane. As shown in the FTIR spectrum in Fig. 2a, the vibration frequency associated with Fe−O is at 586 $cm^{-1}$. The peak at 1420 $cm^{-1}$ is due to C−H bending vibration and the broad peak between 1480 and 1760 $cm^{-1}$ represents the stretching vibration of C−C, C=C, and C=O bonds in the oleic acid carbon chain and carboxyl groups. The oleic acid hydrocarbon chain exhibits distinct C−H stretching at 2830–2950 $cm^{-1}$. All of the peaks can be assigned to oleic-acid stabilized $Fe_3O_4$ nanoparticles [45].

The transmission electron microscopy (TEM) image in Fig. 5a reveals particles with a diameter of 12 nm and a uniform distribution, although minor aggregation can be observed. This is consistent with the DLS results (Fig. 5e) that the size distribution is narrow and average size is around 15 nm. The crystal structure and phase of the magnetic nanoparticles are assessed by XRD and according to Fig. 6a, the diffraction pattern of $Fe_3O_4$ at $2\theta$ of 30.2°, 35.6°, 43.4°, 53.4°, 57.4°, and 62.9° corresponds to the (220), (311), (400), (511), (440), (533) reflection planes of face-centered cubic $Fe_3O_4$, respectively [46] that can be indexed to the standard card of $Fe_3O_4$ (JCPDS 87-2334).

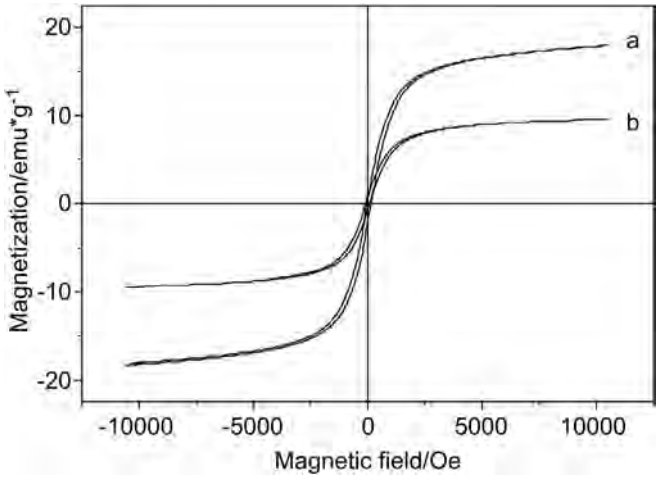


**Fig. 7.** Magnetic hysteresis loops: (a) Oleic acid modified $Fe_3O_4$ nanoparticles and (b) $Fe_3O_4$-encapsulated polymeric micelles.

The amphiphilic poly(HFMA-co-VBK)-g-PEG copolymers show a tendency to form core–shell micelles in water, as shown by the TEM image in Fig. 5b. The water-soluble PEG chains serve as an outer hydrophilic shell stabilizing the micelles and VBK contributes to the fluorescent characteristics. Because of the hydrophobic characteristic of the fluorinated segments, during the self-assembly process, they have a high tendency to bury themselves into the interior of the micelles formed with a hydrophobic core. The morphology of the $Fe_3O_4$-encapsulated polymeric micelles is displayed in Fig. 5c. Isolated magnetite clusters consisting of several tens of densely packed monodispersed magnetite nanocrystals are found. The magnetite clusters are located in the core of the amphiphilic poly(HFMA-co-VBK)-g-PEG copolymer micelles, although the copolymers cannot be discerned by TEM due to the low contrast. In the high-magnification image (Fig. 5d), the detailed structure of the iron oxide in the micelles becomes clearer. Many magnetic nanoparticles aggregate forming small balls which can

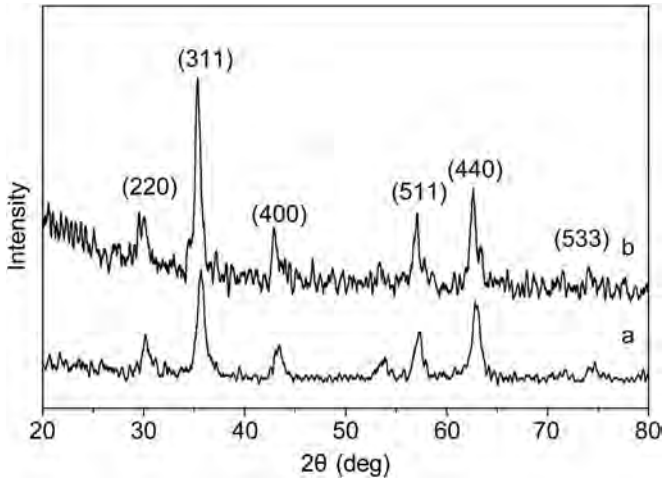


**Fig. 6.** X-Ray powder diffraction patterns: (a) Oleic acid modified $Fe_3O_4$ nanoparticles and (b) $Fe_3O_4$-encapsulated polymeric micelles.

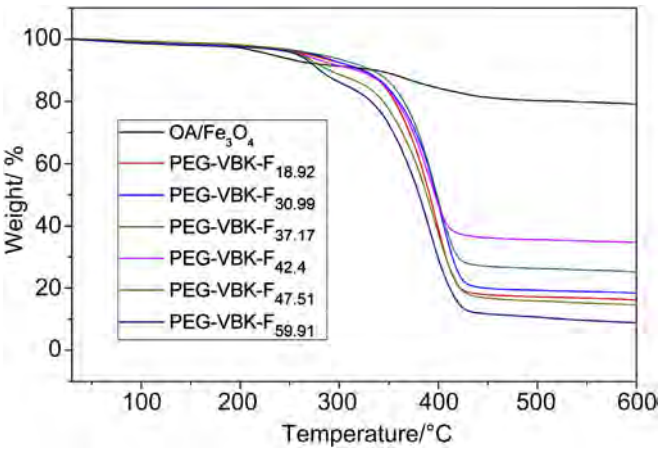


**Fig. 8.** TGA cures of oleic acid stabilized $Fe_3O_4$ nanoparticles and amphiphilic copolymers (PEG–VBK–$F_{18.92}$ to PEG–VBK–$F_{59.91}$).

**Table 1**
Magnetic nanoparticles encapsulation efficiency of different types of amphiphilic poly(HFMA-co-VBK)-g-PEG copolymers.

| Sample code | HFMA (g) | PEGMA (g) | VBK (g) | THF (mL) | AIBN (g) | PFMA (wt.%) | Encapsulation efficiency[a] (wt.%) | Encapsulation efficiency[b] (wt.%) |
|---|---|---|---|---|---|---|---|---|
| 1 | 0.258 | 1.004 | 0.101 | 12 | 0.068 | 18.92 | 17.18 | 17.55 |
| 2 | 0.456 | 1.005 | 0.101 | 12 | 0.068 | 30.99 | 19.47 | 19.92 |
| 3 | 0.655 | 1.005 | 0.102 | 12 | 0.068 | 37.17 | 26.34 | 26.92 |
| 4 | 0.815 | 1.005 | 0.102 | 12 | 0.068 | 42.4 | 35.71 | 36.02 |
| 5 | 1.002 | 1.004 | 0.103 | 12 | 0.068 | 47.51 | 15.82 | 16.18 |
| 6 | 1.516 | 1.004 | 0.101 | 12 | 0.068 | 59.91 | 11.07 | 11.54 |

[a] Encapsulation efficiency is determined by TGA.
[b] Encapsulation Efficiency is determined by atomic absorption spectrophotometry.

enter the hydrophobic core of the amphiphilic poly(HFMA-co-VBK)-g-PEG copolymers micelles because of the intermolecular force between oleic acid and copolymers. The hydrodynamic size of the $Fe_3O_4$-encapsulated polymeric micelles is also measured by DLS and the results are shown in Fig. 5f. The magnetite-loaded micelles have a diameter of 146 nm and the size distribution is quite narrow. They are stable and do not aggregate in water. The XRD pattern acquired from the $Fe_3O_4$-encapsulated polymeric micelles in Fig. 6b shows the same peaks as $Fe_3O_4$. Compared to Fig. 2b, the FTIR spectrum of the $Fe_3O_4$-encapsulated polymeric micelles (Fig. 2c) shows a wide absorption peak at 586 $cm^{-1}$ suggesting the presence of $Fe_3O_4$. These results confirm that $Fe_3O_4$ nanoparticles are incorporated into the polymeric micelles and magnetite clusters with copolymer shells form during self-assembly.

### 3.3. Magnetic and thermal properties

To determine the magnetic property of oleic acid stabilized $Fe_3O_4$ and $Fe_3O_4$-encapsulated polymeric micelles, the magnetic properties of the powders are evaluated by vibrating sample magnetometer (VSM) at room temperature. Fig. 7 presents a typical plot of magnetization versus applied magnetic field, and the absence of the hysteresis loop confirms that both the $Fe_3O_4$ nanoparticles and $Fe_3O_4$-encapsulated polymeric micelles possess good super-magnetic properties. The saturation magnetization values (Ms) of the oleic acid-stabilized $Fe_3O_4$ nanoparticles and $Fe_3O_4$-encapsulated polymeric micelles are 18.13 emu/g and 9.61 emu/g, respectively. Loss of magnetization is due to the presence of the copolymers surrounding the magnetic cores, partial oxidation effects on the magnetic nanoparticles, and decrease in the magnetite fraction in each composite [47]. Fig. 8 shows the TGA curves of the oleic acid stabilized $Fe_3O_4$ nanoparticles and $Fe_3O_4$-encapsulated polymeric micelles fabricated with a series of copolymers of different HFMA/(PEGMA + VBK) ratios. The TGA curve of the oleic acid-stabilized $Fe_3O_4$ nanoparticles shows a weight loss of OA on $Fe_3O_4$. The total weight loss is about 19.3% in the temperature range between 160 and 450 °C. All the $Fe_3O_4$-encapsulated polymeric micelles with different HFMA/(PEGMA + VBK) mass ratios exhibit two different weight losses. The first stage between 160 and 350 °C arises from degradation of oleic acid and polyHFMA whereas the second on between 350 and 450 °C stems from decomposition of PEG and VBK on the surface of the $Fe_3O_4$ nanoparticles. The $Fe_3O_4$ content in the different polymeric micelles calculated from the TGA results is: PEG–VBK–$F_{18.92}$ (17.18%), PEG–VBK–$F_{30.99}$ (19.47%), PEG–VBK–$F_{37.17}$ (26.34%), PEG–VBK–$F_{42.4}$ (35.7%), PEG–VBK–$F_{47.51}$ (15.8%), and PEG–VBK–$F_{59.91}$ (11.07%). The results are basically in accordance with those obtained by atomic absorption spectrophotometry shown in Table 1. Generally, the $Fe_3O_4$ contents calculated by TGA are slightly less than those by atomic absorption and this discrepancy may be due to oxidation, decomposition, and other effects. With increasing fluorine content in the amphiphilic poly(HFMA-co-VBK)-g-PEG copolymers, the loading efficiency of magnetic nanoparticles increases initially but

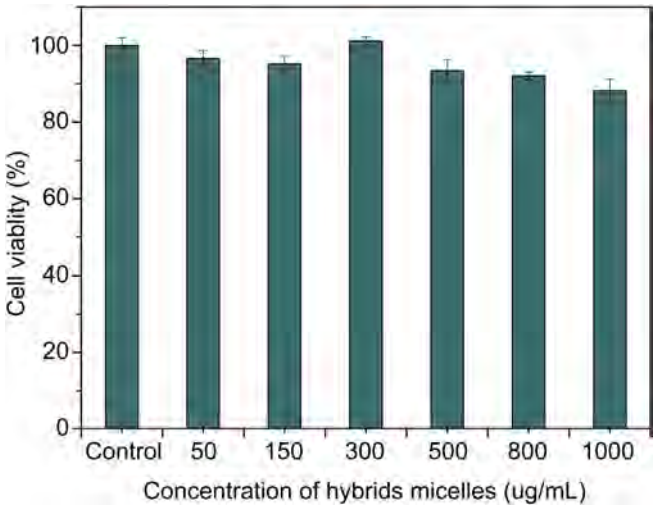


**Fig. 9.** Cell viability of HeLa cells treated with different concentrations of hybrid micelles.

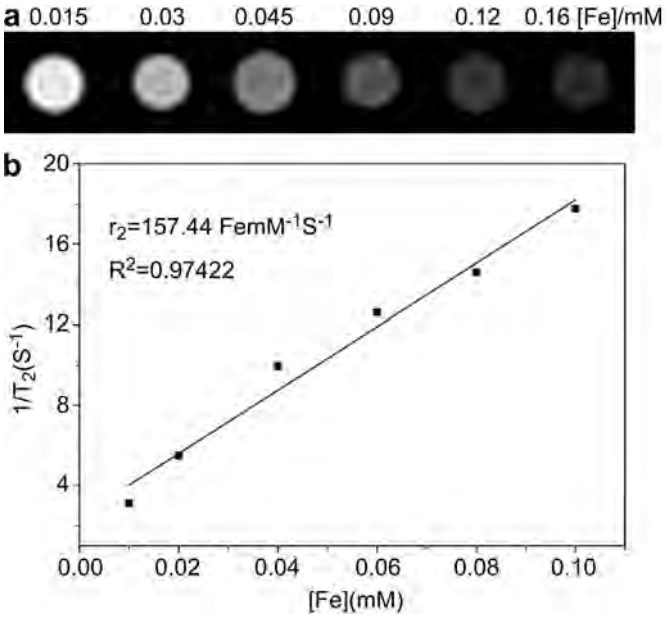


**Fig. 10.** (a) $T_2$-weight MR images of the aqueous solution containing hybrids micelles and different iron concentrations and (b) $T_2$-relaxation rate ($1/T_2$) as a function of iron concentrations for the hybrid micelles.

begins to decline when the fluorine concentration reaches a certain level [48].

### 3.4. In vitro cytotoxicity

To evaluate the *in vitro* cytotoxicity of $Fe_3O_4$-encapsulated polymeric micelles, the MTT assay is performed on HeLa cell lines. The cells with different concentrations are incubated on the $Fe_3O_4$-encapsulated polymeric micelles for 24 h. As shown in Fig. 9, the cell viability is over 90% at a concentration of 800 μg/mL, suggesting good cytocompatibility at this concentration. The $Fe_3O_4$-encapsulated polymeric micelles are thus cytocompatible up to a $Fe_3O_4$-encapsulated polymeric micelle concentration of 1 mg $mL^{-1}$, thus boding well for biomedical applications.

### 3.5. Relaxivity and in vivo MRI

$Fe_3O_4$ nanoparticles are good $T_2$ contrast agents in MRI. To investigate the efficacy of the $Fe_3O_4$-encapsulated polymeric micelles, the $T_2$-weighted images of the $Fe_3O_4$-encapsulated polymeric micelles for different Fe concentrations (0.015–0.16 mM/L) are acquired on a clinical 3T MRI instrument. As shown in Fig. 10a, small iron content shows a bright white $T_2$-weighed MR image and the MR signal declines with increasing content of $Fe_3O_4$-encapsulated polymeric micelles, confirming the capability of the $Fe_3O_4$-encapsulated polymeric micelles to enhance the transverse proton relaxation process.

Super-paramagnetic $Fe_3O_4$ nanoparticles are usually used as MR negative contrast agents and so the $Fe_3O_4$-encapsulated polymeric

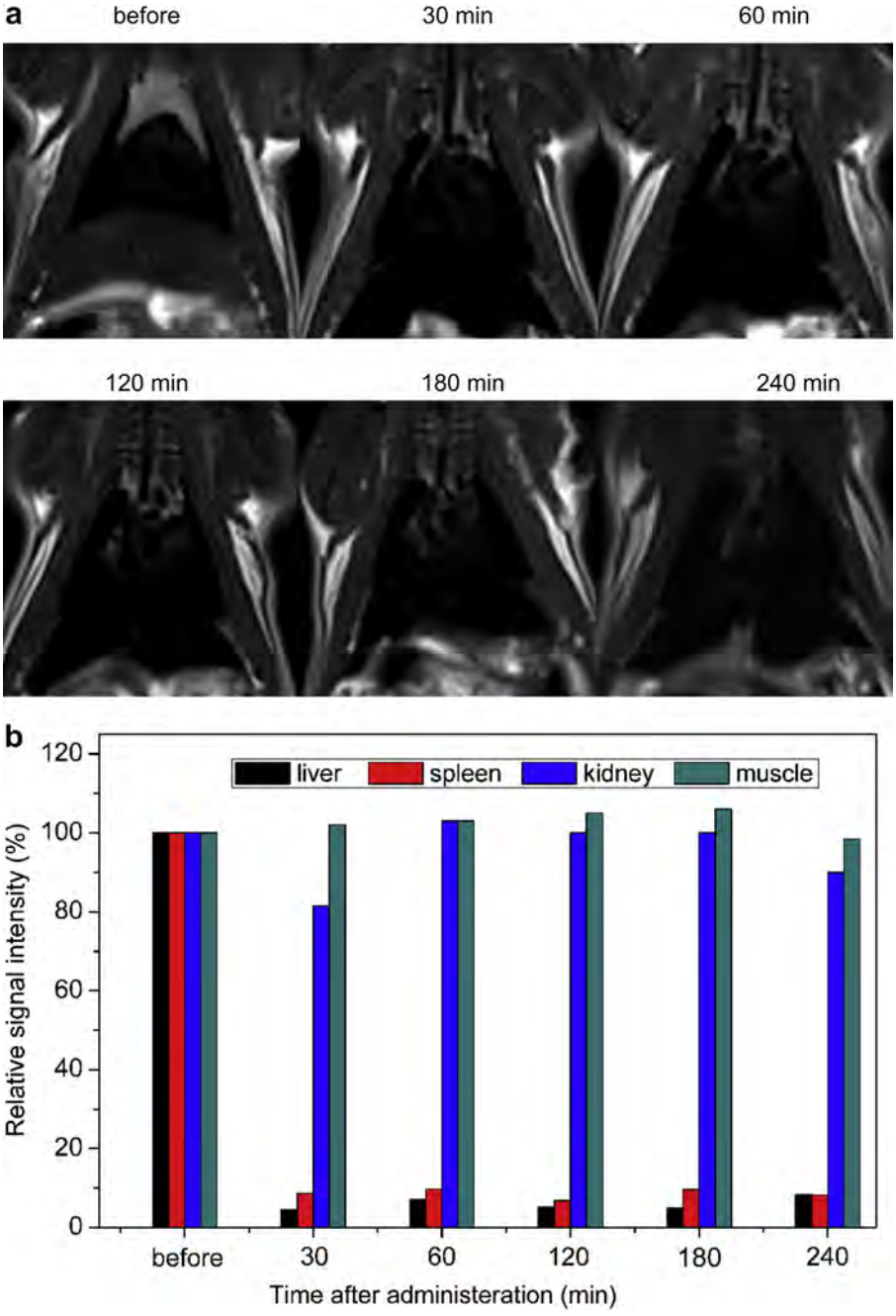


**Fig. 11.** (a) $T_2$-weighted images of mice at different time points before and after tail vein administration of the hybrid micelles and (b) Relative signal enhancement values of the liver, kidney, spleen, and muscle before and after injection of hybrid micelles.

micelles are evaluated based on the relaxivity parameter ($r_2$) using an MRI scanner. The same concentration range is investigated for $r_2$ calculated from the slope of the concentration-dependent relaxation rate $1/T_2$ graphs. As shown in Fig. 10b, a good linear relationship is observed when the Fe molar concentration is plotted against $r_2$. According to the slope, $r_2$ of the $Fe_3O_4$-encapsulated polymeric micelles is calculated to be 157.44 $mM^{-1}$ $S^{-1}$, indicating that the $Fe_3O_4$-encapsulated polymeric micelles have negative contrast effect and can be used as an MRI negative contrast agent.

In order to evaluate the *in vivo* $T_2$-weighted MR imaging capability, SD mice models undergo tail vein injection of the $Fe_3O_4$-encapsulated polymeric micelles and the MR images are acquired from the mice at scheduled time points. Before injecting the micelles, the liver is seen as the hyperintense area in the $T_2$-weighted MR images. At 30 min post-injection, significant darkening can be observed from the liver area of the $T_2$-weighted MR image (Fig. 11a) and this high contrast of the liver tissue persists during observation for 240 min.

Generally, magnetic nanoparticles modified by PEGs are often uptaken by the reticuloendothelial system (RES) [48], which can be used in liver and spleen MR imaging. The signal intensity change in the organs reflects iron accumulation. As shown in Fig. 11b, the liver and spleen contrast is enhanced significantly 30 min after injection of the hybrid micelles. The relative SI in the rat liver and spleen is reduced by 92.96% and 90.36% at 30 min post-injection, respectively. The high contrast of the liver and spleen persists for 4 h. It is due to the large hybrid micelles concentrations in these organs and considerable sequestration of the hybrid micelles by the macrophages of RES. On the contrary, no significant RSE change is observed from the kidney and muscle furnishing evidence that the materials do not permeate these organs.

To better understand the particle pharmacokinetics, Prussian blue staining is performed on the major organ dissections. The slides of different organs including the liver, spleen, kidney, and muscle are further examined by *ex vivo* Prussian blue staining extracted from the mouse immediately after *in vivo* MR imaging at 10 h post-injection. As shown in Fig. 12a and b, some parts of the liver and spleen are stained blue (in web version), indicating the presence or accumulation of iron oxide in these areas, but it is difficult to find blue dots in the kidney and muscles (Fig. 12c and d). The results suggest that the hybrid micelles can be used as a negative MR contrast agent for the liver and spleen.

### 3.6. Fluorescence and in vivo fluorescent imaging

Carbazole which emits in the blue delivers more stable fluorescence intensity and versatile structural derivatization than other dyes [49]. The carbazole segments synthesized by the Michael-type reaction are attached to the amphiphilic copolymers. Introduction of the blue emitting segments yields excellent fluorescent property making the materials suitable as an optical probe in the biological microenvironment. The concentration-dependent fluorescence emission spectra of amphiphilic poly(HFMA-co-VBK)-g-PEG copolymers in deionized water are acquired under excitation at 294 nm and two emission peaks at 350 and 365 nm are shown in Fig. 13a. As the concentration of the copolymers increases from 0.01 to 0.24 g/L, the intensity of two peaks increases, indicating that the amphiphilic poly(HFMA-co-VBK)-g-PEG copolymer at a high concentration can produce detectable signals suitable for optical imaging. The fluorescent properties of the $Fe_3O_4$-encapsulated polymeric micelles are also evaluated by recording the emission spectra for various concentrations. The fluorescence intensity increases initially as the concentration of $Fe_3O_4$-encapsulated polymeric micelles increases from 0.01 mM/L to 0.2 mM/L (Fig. 13b), but then decreases when the concentration increases further to 0.9 mM/L (Fig. 13c) resulting from fluorescence self-quenching and magnetism of $Fe_3O_4$ [32]. Therefore,

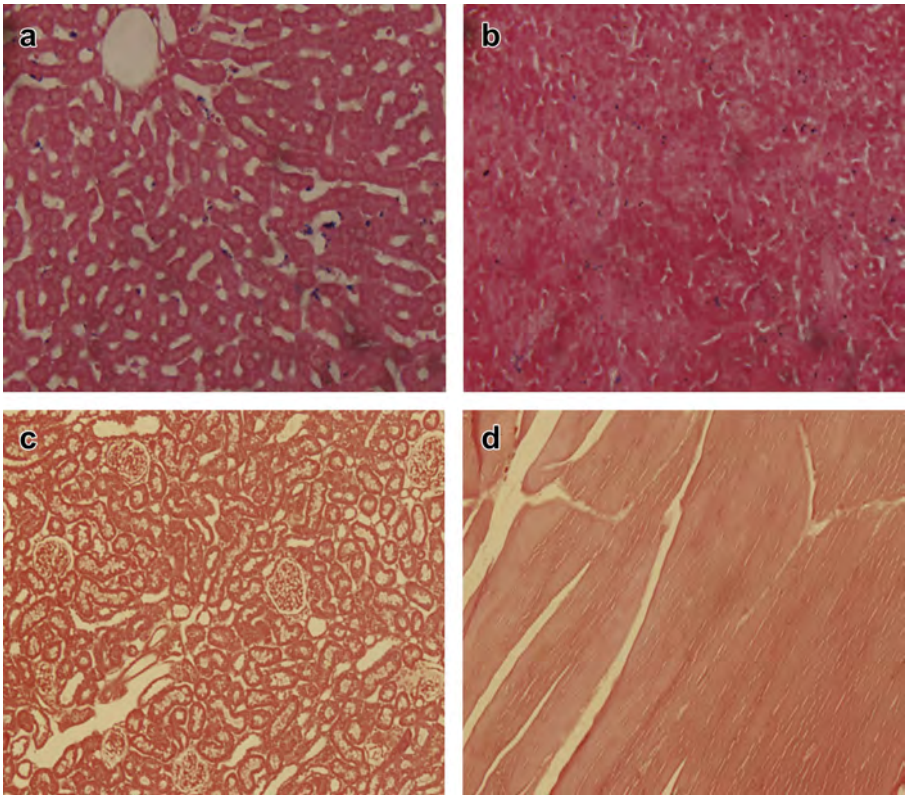


**Fig. 12.** Prussian blue stained images: (a) Liver, (b) Spleen, (c) Kidney, and (d) Muscle after 10 h tail vein injection of hybrid micelles.

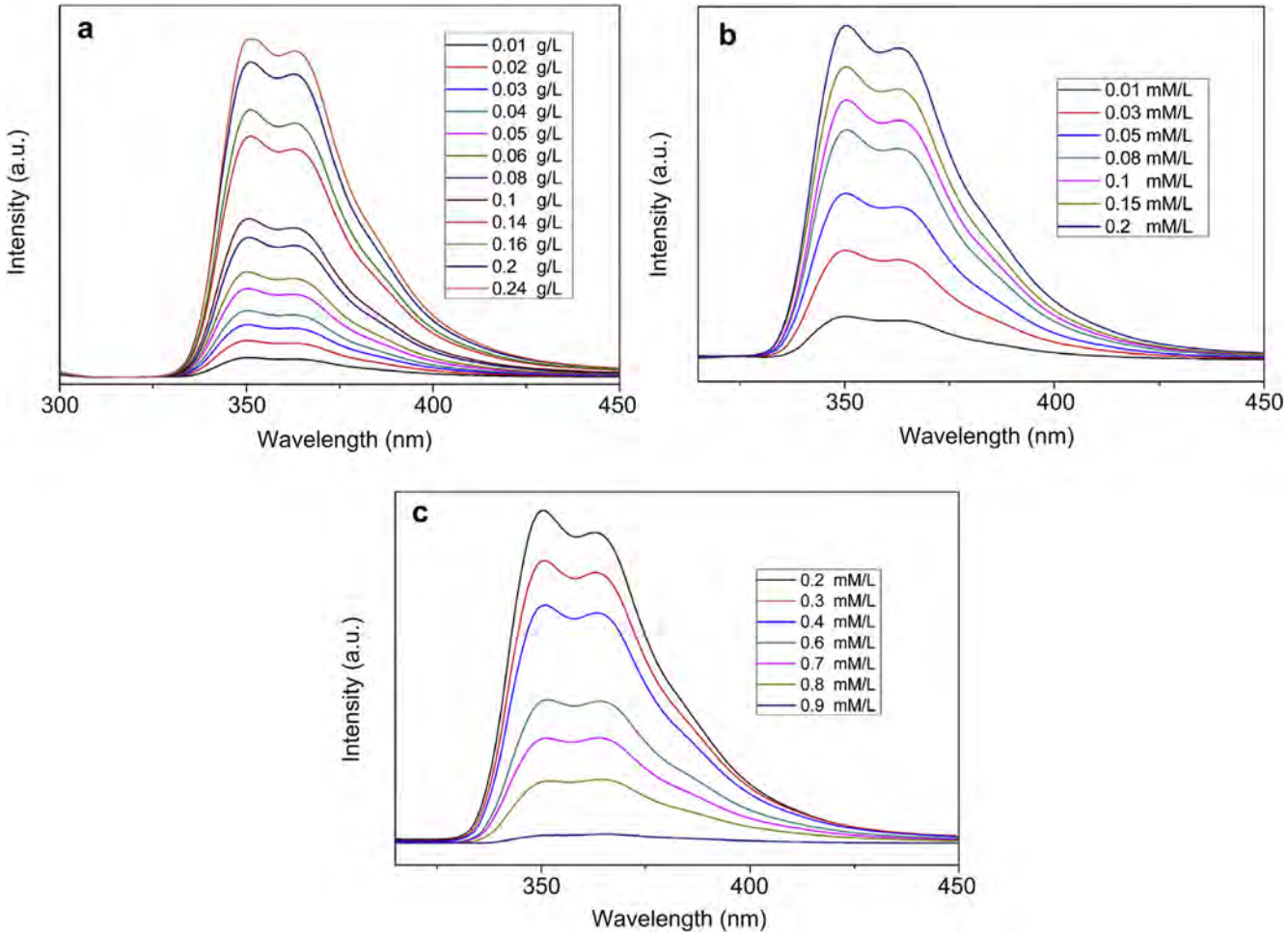


**Fig. 13.** Fluorescence spectra: (a) Amphiphilic poly(HFMA-co-VBK)-g-PEG copolymers, (b and c) Hybrid micelles in water with different concentrations at room temperature excited by 294 nm.

the suitable concentration of the $Fe_3O_4$-encapsulated polymeric micelles for optical imaging is 0.2 mM/L.

To further assess the optical properties of the amphiphilic poly(HFMA-co-VBK)-g-PEG copolymers, the CLSM images are obtained by 2-photon (690–1040 nm) laser confocal microscopy (Carl Zeiss LSM710). The copolymers exhibit characteristic vivid blue (in web version) fluorescence derived from carbazole under 2-photon 690 nm laser irradiation (Fig. 14b), but the copolymers do not show any fluorescence under natural light (Fig. 14a). Vivid blue (in web version) fluorescence is still shown in the overlapped images obtained using the two light sources (Fig. 14c) confirming the excellent fluorescent properties.

The fluorescence intensities from several organs are monitored *ex vivo* to confirm accumulation of $Fe_3O_4$-encapsulated polymeric micelles. As shown in Fig. 15, no fluorescence is observed from the liver (Fig. 15a) and spleen (Fig. 15b) without the $Fe_3O_4$-encapsulated polymeric micelles. In contrast, the color map of the fluorescent image shows more details about the organ signals. Intense fluorescence is observed from the $Fe_3O_4$-encapsulated polymeric micelles in the liver (Fig. 15c) and spleen (Fig. 15d). The results clearly

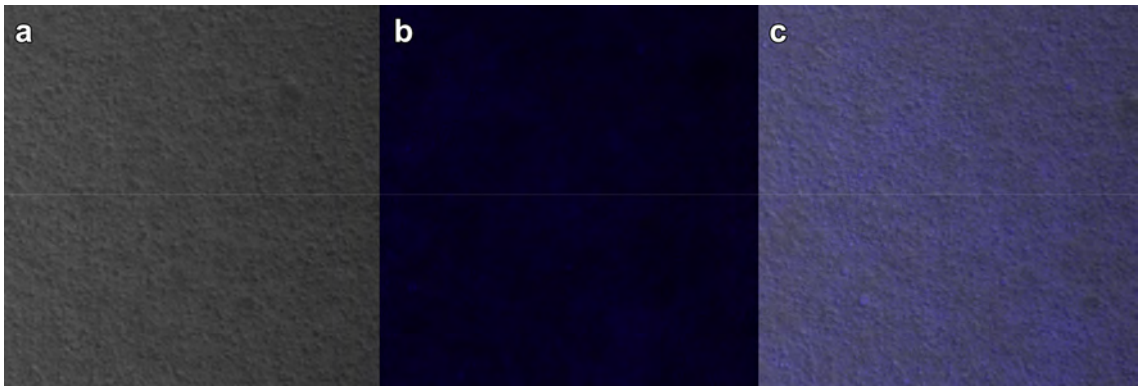


**Fig. 14.** CLSM images of amphiphilic poly(HFMA-co-VBK)-g-PEG copolymers: (a), (b) Under 2-photon 690 nm laser irradiation, (c) Overlap of (a) and (b).

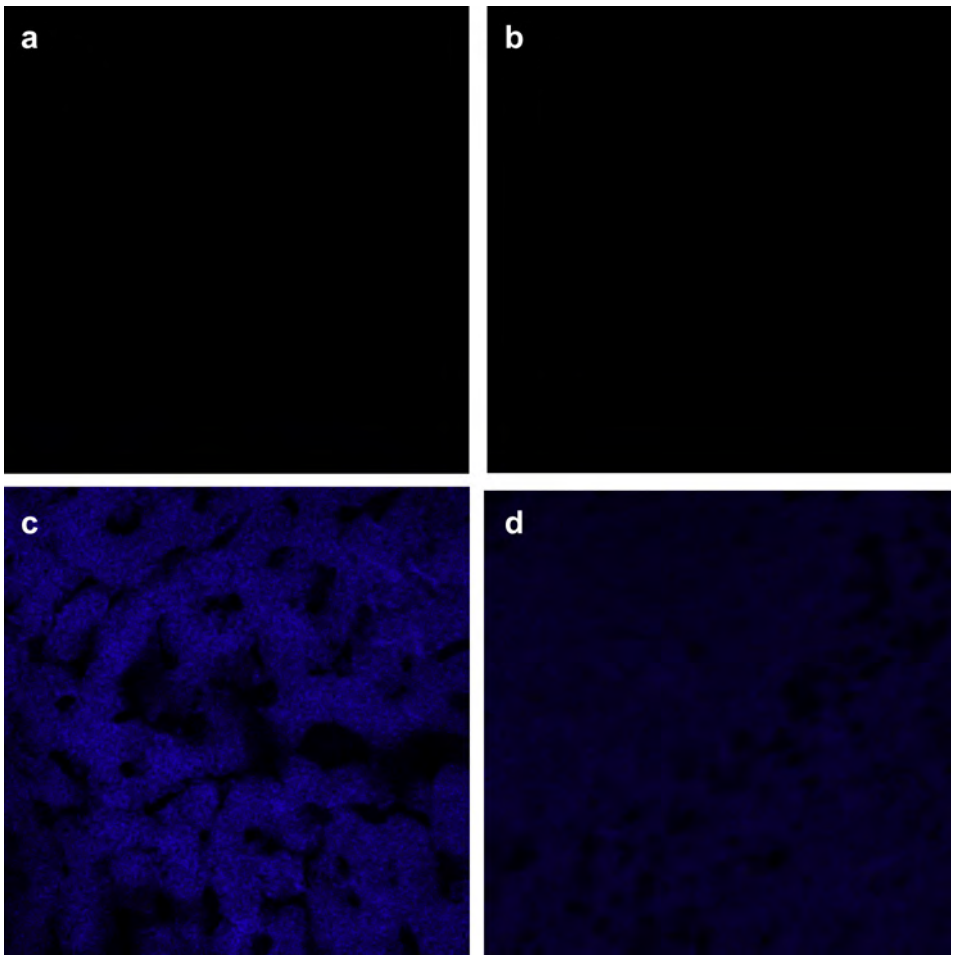


**Fig. 15.** CLSM images: (a) Liver and (b) Spleen after injected with saline solution; (c) Liver and (d) Spleen after injection with hybrid micelles.

show accumulation of $Fe_3O_4$-encapsulated polymeric micelles in these organs and moreover, relatively weak fluorescence is observed from the $Fe_3O_4$-encapsulated polymeric micelles in the spleen compared to the liver. This phenomenon can be attributed to the stronger phagocytosis of the liver than spleen.

## 4. Conclusion

Stable and cytocompatible multifunctional hybrid PEGylated micelles are described. The $F_3O_4$-encapsulated polymeric micelles composed of cores containing magnetic nanoparticles as well as polyethylene glycol (PEG) shells are synthesized by self-assembly of amphiphilic poly(HFMA-co-VBK)-g-PEG copolymers and oleic acid stabilized $Fe_3O_4$ nanoparticles. The $Fe_3O_4$-encapsulated polymeric micelles have a hydrodynamic diameter of 146 nm and excellent paramagnetic properties with a maximum saturation magnetization of 9.61 emu/g and transverse relaxivity rate of 157.44 $m_M^{-1}\,S^{-1}$. They are demonstrated to be an appropriate dual-imaging probe with blue fluorescence and MR imaging for the liver and spleen. The hybrid micelles have large clinical potential in magnetic resonance imaging and optical imaging.

## Acknowledgments

This work was supported by the National Natural Science Foundation of China (Grant No. 51273058). This work was supported, in part, by National 973 Program of China (Grant No. 2011CB933103), Hong Kong Research Grants Council (RGC), General Research Funds CityU 112212, and City University of Hong Kong Applied Research Grant (ARG) No. 9667066.

## References

[1] Qiao RR, Yang CH, Gao MY. Superparamagnetic iron oxide nanoparticles: from preparations to *in vivo* MRI applications. J Mater Chem 2009;19:6274–93.
[2] Tanaka T, Sakai R, Kobayashi R, Hatakeyama K, Matsunaga T. Contributions of phosphate to DNA adsorption/desorption behaviors on aminosilane-modified magnetic nanoparticles. Langmuir 2009;25:2956–61.
[3] Zeng H, Li J, Wang ZL, Liu JP, Sun SH. Bimagnetic core/shell FePt/$Fe_3O_4$ nanoparticles. Nano Lett 2004;1:187–90.
[4] Kievit FM, Zhang M. Surface engineering of iron oxide nanoparticles for targeted cancer therapy. Acc Chem Res 2011;44:853–62.
[5] Laurent S, Forge D, Port M, Roch A, Robic C, Elst LV, et al. Magnetic iron oxide nanoparticles synthesis, stabilization, vectorization, physicochemical characterizations, and biological applications. Chem Rev 2008;108:2064–110.
[6] Lee J, Lee N, Kim H, Kim J, Choi S, Kim J, et al. Uniform mesoporous dye-doped silica nanoparticles decorated with multiple magnetite nanocrystals for simultaneous enhanced magnetic resonance imaging, fluorescence imaging, and drug delivery. J Am Chem Soc 2010;132:552–7.
[7] Yang H, Zhang CX, Shi XY, Hu H, Du XX, Fang Y, et al. Water-soluble superparamagnetic manganese ferrite nanoparticles for magnetic resonance imaging. Biomaterials 2010;31:3667–73.
[8] Liu Y, Welch MJ. Nanoparticles labeled with positron emitting nuclides: advantages, methods, and applications. Bioconjug Chem 2012;23:671–82.
[9] Kim J, Piao YZ, Hyeon T. Multifunctional nanostructured materials for multimodal imaging, and simultaneous imaging and therapy. Chem Soc Rev 2009;38:372–90.
[10] Sun Y, Yu M, Liang S, Zhang Y, Li C, Mou T, et al. Fluorine-18 labeled rare-earth nanoparticles for positron emission tomography (PET) imaging of sentinel lymph node. Biomaterials 2011;32:2999–3007.
[11] Xu ZH, Li CX, Kang XJ, Yang DM, Yang P, Hou ZY, et al. Synthesis of a multifunctional nanocomposite with magnetic, mesoporous, and near-IR absorption properties. J Phys Chem C 2010;114:16343–50.

[12] Yan K, Li PH, Zhu HE, Zhou YJ, Ding JD, Shen J, et al. Recent advances in multifunctional magnetic nanoparticles and applications to biomedical diagnosis and treatment. RSC Adv 2013;3:10598–618.
[13] Khemtong C, Kessinger CW, Gao J. Polymeric nanomedicine for cancer MR imaging and drug delivery. Chem Commun 2009;24:3497–510.
[14] Devaraj NK, Keliher EJ, Thurber GM, Nahrendorf M, Weissleder R. $^{18}$F labeled nanoparticles for *in vivo* PET-CT imaging. Bioconjug Chem 2009;20:397–401.
[15] Zhu X, Zhou J, Chen M, Shi M, Feng W, Li F. Core-shell $Fe_3O_4$@$NaLuF_4$:Yb, Er/Tm nanostructure for MRI, CT and upconversion luminescence tri-modality imaging. Biomaterials 2012;33:4618–27.
[16] Torres Martin de Rosales R, Tavare R, Paul RL, Jauregui-Osoro M, Protti A, Glaria A, et al. Synthesis of $^{64}$Cu(II)-bis(dithiocarbamatebisphosphonate) and its conjugation with superparamagnetic iron oxide nanoparticles: *in vivo* evaluation as dual-modality PET-MRI agent. Angew Chem Int Ed 2011;50:5509–13.
[17] Shi D, Cho HS, Chen Y, Xu H, Gu H, Lian J, et al. Fluorescent polystyrene-$Fe_3O_4$ composite nanospheres for *in vivo* imaging and hyperthermia. Adv Mater 2009;21:2170–3.
[18] Xie J, Chen K, Huang J, Lee S, Wang J, Gao J, et al. PET/NIRF/MRI triple functional iron oxide nanoparticles. Biomaterials 2010;31:3016–22.
[19] Zhou J, Yu M, Sun Y, Zhang X, Zhu X, Wu Z, et al. Fluorine-18-labeled $Gd^{3+}$/$Yb^{3+}$/$Er^{3+}$ co-doped $NaYF_4$ nanophosphors for multimodality PET/MR/UCL imaging. Biomaterials 2011;32:1148–56.
[20] Xing H, Bu W, Zhang S, Zheng X, Li M, Chen F, et al. Multifunctional nanoprobes for upconversion fluorescence, MR and CT trimodal imaging. Biomaterials 2012;33:1079–89.
[21] Tong L, Shi J, Liu D, Li Q, Ren X, Yang H. Luminescent and magnetic properties of $Fe_3O_4$@$SiO_2$@$Y_2O_3$:$Eu^{3+}$ composites with core–shell structure. J Phys Chem C 2012;116:7153–7.
[22] Wang C, Irudayaraj J. Multifunctional magnetic-optical nanoparticle probes for simultaneous detection, separation, and thermal ablation of multiple pathogens. Small 2010;6:283–9.
[23] Na HB, Song IC, Hyeon T. Inorganic nanoparticles for MRI contrast agents. Adv Mater 2009;21:2133–48.
[24] Lee N, Choi Y, Lee Y, Park M, Moon WK, Choi SH, et al. Water-dispersible ferrimagnetic iron oxide nanocubes with extremely high r(2) relaxivity for highly sensitive *in vivo* MRI of tumors. Nano Lett 2012;12:3127–31.
[25] Cheng D, Hong G, Wang W, Yuan R, Ai H, Shen J, et al. Nonclustered magnetite nanoparticle encapsulated biodegradable polymeric micelles with enhanced properties for *in vivo* tumor imaging. J Mater Chem 2011;21:4796–804.
[26] Li Z, Chen H, Bao HB, Gao MY. One-pot reaction to synthesize water-soluble magnetite nanocrystals. Chem Mater 2004;16:1391–3.
[27] Kura H, Takahashi M, Ogawa T. Synthesis of monodisperse iron nanoparticles with a high saturation magnetization using an Fe(CO)x-oleylamine reacted precursor. J Phys Chem C 2010;114:5835–8.
[28] Sun SH, Zeng H. Size-controlled synthesis of magnetite nanoparticles. J Am Chem Soc 2002;124:8204–5.
[29] Palma R, Peeters S, Bael M, Rul H, Bonroy K, Laureyn W. Silane ligand exchange to make hydrophobic superparamagnetic nanoparticles water-dispersible. Chem Mater 2007;19:1821–31.
[30] Hu F, Neoh KG, Kang ET. Synthesis of folic acid functionalized PLLA-b-PPEGMA nanoparticles for cancer cell targeting. Macromol Rapid Commun 2009;30:609–14.
[31] Kim J, Lee JE, Lee SH, Yu JH, Lee JH, Park TG, et al. Designed fabrication of a multifunctional polymer nanomedical platform for simultaneous cancer-targeted imaging and magnetically guided drug delivery. Adv Mater 2008;20:478–83.
[32] Gao G, Heo H, Lee J, Lee D. An acidic pH-triggered polymeric micelle for dual-modality MR and optical imaging. J Mater Chem 2010;20:5454–61.
[33] Hickey RJ, Haynes AS, Kikkawa JM, Park SJ. Controlling the self-assembly structure of magnetic nanoparticles and amphiphilic block-copolymers: from micelles to vesicles. J Am Chem Soc 2011;133:1517–25.
[34] Kim B, Qiu J, Wang J, Taton T. Magnetomicelles: composite nanostructures from magnetic nanoparticles and cross-linked amphiphilic block copolymers. Nano Lett 2005;5:1987–91.
[35] Ai H, Flask C, Weinberg B, Shuai X, Pagel M, Farrel D, et al. Magnetite-loaded polymeric micelles as ultrasensitive magnetic-resonance probes. Adv Mater 2005;17:1949–52.
[36] Panthi K, Adhikari RM, Kinstle TH. Carbazole donor–carbazole linker-based compounds: preparation, photophysical properties, and formation of fluorescent nanoparticles. J Phys Chem A 2010;114:4550–7.
[37] Kaeser A, Fischer I, Abbel R, Besenius P, Dasgupta D, Gillisen MAJ, et al. Side chains control dynamics and self-sorting in fluorescent organic nanoparticles. ACS Nano 2013;7:408–16.
[38] Li Q, Zhang L, Bai L, Zhang Z, Zhu J, Zhou N, et al. Multistimuli-responsive hybrid nanoparticles with magnetic core and thermoresponsive fluorescence-labeled shell via surface-initiated RAFT polymerization. Soft Matter 2011;7:6958–66.
[39] Li XL, Li H, Liu GQ, Deng ZW, Wu SL, Li PH, et al. Magnetite-loaded fluorine-containing polymeric micelles for magnetic resonance imaging and drug delivery. Biomaterials 2012;33:3013–24.
[40] Liu J, He W, Zhang L, Zhang Z, Zhu J, Yuan L, et al. Bifunctional nanoparticles with fluorescence and magnetism via surface-initiated AGET ATRP mediated by an iron catalyst. Langmuir 2011;27:12684–92.
[41] Lee S-J, Jeong J-R, Shin S-C, Kim J-C, Kim J-D. Synthesis and characterization of superparamagnetic maghemite nanoparticles prepared by coprecipitation technique. J Magn Magn Mater 2004;282:147–50.
[42] Xiong SD, Li L, Jiang J, Tong LP, Wu S, Xu ZS, et al. Cationic fluorine-containing amphiphilic graft copolymers as DNA carriers. Biomaterials 2010;31:2673–85.
[43] Wang C, Wang ZQ, Shen X. Amphiphilic building blocks for self-assembly: from amphiphiles to supra-amphiphiles. Acc Chem Res 2012;45:608–18.
[44] Burlatsky SF, Atrazhev VV, Dmitriev DV, Sultanov VI, Timokhina EN, Ugolkova EA, et al. Surface tension model for surfactant solutions at the critical micelle concentration. J Colloid Interface Sci 2013;393:151–60.
[45] Puig J, Hoppe CE, Fasce LA, Pérez CJ, Piñeiro-Redondo Y, Bañobre-López M, et al. Superparamagnetic nanocomposites based on the dispersion of oleic acid-stabilized magnetite nanoparticles in a diglycidylether of bisphenol a-based epoxy matrix: magnetic hyperthermia and shape memory. J Phys Chem C 2012;116:13421–8.
[46] Zeng Y, Hao R, Xing B, Hou Y, Xu Z. One-pot synthesis of $Fe_3O_4$ nanoprisms with controlled electrochemical properties. Chem Commun 2010;46:3920–2.
[47] Vestal C, Zhang Z. Synthesis and magnetic characterization of Mn and Co spinel ferrite-silica nanoparticles with tunable magnetic core. Nano Lett 2003;3:1739–43.
[48] Yallapu MM, Othman SF, Curtis ET, Gupta BK, Jaggi M, Chauhan SC. Multifunctional magnetic nanoparticles for magnetic resonance imaging and cancer therapy. Biomaterials 2011;32:1890–905.
[49] Kim SH, Cho I, Sim MK, Park S, Park SY. Highly efficient deep-blue emitting organic light emitting diode based on the multifunctional fluorescent molecule comprising covalently bonded carbazole and anthracene moieties. J Mater Chem 2011;21:9139–48.